The reduction of NO by CO under oxygen-rich conditions in a fixed-bed catalytic reactor: A mathematical model that can explain the peculiar behavior

Alexei G. Makeev*, Nickolai V. Peskov

Faculty of Computational Mathematics and Cybernetics, Lomonosov Moscow State University, Moscow 119991, Russia

ARTICLE INFO

ABSTRACT

A kinetic model of the $NO + CO + O_2$ catalytic reaction in the isothermal continuous stirred tank reactor (CSTR) has been introduced previously in [A.G. Makeev, N.V. Peskov, H. Yanagihara, Appl. Catal. B: Environ. 119–120 (2012) 273]. The present study implements the same kinetic mechanism but now it is combined with a more realistic model of the catalytic flow reactor – the axially dispersed plug flow reactor model. The resulting new model is compared with the CSTR-based model. The calculations demonstrate that back-mixing in the isothermal reactor can lead to the following effect. At sufficiently high temperatures, when the conversion of CO is close to 100%, an increase in NO-to-N_2 conversion can be induced by: (1) the decrease of the active catalyst surface area and (2) the increase of the space velocity of the feed gas. These items just represent the peculiar behavior, which seems to contradict with the physical intuition. In fact, such results have been observed experimentally, but probably they have not been properly explained. We demonstrate that these peculiar effects can be caused by the kinetics of competing reactions in a catalytic flow reactor. The vital step in the reaction mechanism appears to be the *reversible* dissociation of the adsorbed NO species. In particular, the calculations show that the overall reactor efficiency can decrease significantly when the catalyst surface area is increasing. This effect disappears if the ideal plug flow model (i.e., without dispersion/diffusion) is applied.

1. Introduction

Millions of tons of toxic NO are produced each year in the world because NO is an intermediate in the Ostwald process for the synthesis of nitric acid from ammonia and oxygen. In the chemical industry, the selective oxidation of ammonia with air over Pt/Rh catalyst at temperatures above 1000 K gives the NH_3-to-NO conversion of up to 98%. The same noble metals are used in three-way catalytic converters, but here they perform the opposite task: catalytic reduction of NO and NO_2 (de-NO_x). N_2 is a required product for the de-NO_x reaction, but it is an undesired reaction product in the Ostwald process. N_2O is an unwanted by-product in both cases. The catalytic converter can work very well in assisting the conversion of NO to N_2, but it becomes ineffective under oxygen-rich (lean-burn) conditions. Selective catalytic reduction (SCR) of NO by CO, hydrocarbons (C_xH_y), H_2 and NH_3 has been extensively studied during the last 25 years in an attempt to overcome this problem [1,2]. At present, NH_3-SCR is widely used for NO_x abatement from stationary sources. Ammonia/urea SCR systems, possibly in combination with the NO_x storage-reduction (NSR) technology, are becoming one of the favored choices for mobile applications [2].

The individual reactions involved in the de-NO_x process on noble metals, which are accepted by most researchers (e.g., in Refs. [3–8]), include the dissociation of adsorbed NO (NO_{ads}) and recombination of two nitrogen adatoms to give N_2 or a nitrogen adatom with NO_{ads} to give N_2O. The dissociation of NO_{ads} is thought to be the most crucial step in the NO reduction process. The main role of CO (and/or C_xH_y, NH_3, H_2) in this case is to remove adsorbed oxygen from a catalyst surface in order to allow for the adsorption and dissociation of NO_{ads}. Also, it is generally accepted that adsorbed oxygen strongly inhibits the rate of NO decomposition [4,7,9], for example, by occupying vacant sites required for NO adsorption and dissociation. Therefore, the usual catalytic convertor becomes ineffective for NO_x reduction in the presence of excess oxygen. To our opinion, this explanation is correct but not complete. The experimental findings and first-principle density functional theory (DFT) calculations (e.g., see Refs. [10,11] for the Pt(1 0 0) surface) indicate that the dissociation of NO_{ads} into N_{ads} and O_{ads} is essentially a reversible process: N_{ads} and O_{ads} can assemble back into NO_{ads}. Therefore, we suppose that the following elementary reaction is one of the most important reactions both for the Ostwald process and for SCR of NO_x:

$$NO_{ads} + (*) \leftrightarrow N_{ads} + O_{ads},$$

* Corresponding author. Tel.: +7 495 9394079; fax: +7 495 9392596.
E-mail addresses: amak@cs.msu.su (A.G. Makeev), peskov@cs.msu.su (N.V. Peskov).

Notation

D_b	axial diffusion coefficient of type b species ($m^2 s^{-1}$)
$\bar{D}_b$	($=D_b/L^2$) normalized diffusion coefficient (s^{-1})
E_i	activation energy of step i (J/mol)
F	volumetric flow rate ($m^3 s^{-1}$)
h	($=N^{-1}$) grid spacing
k_B	Boltzmann constant (J/K)
k_i	reaction rate coefficient of step i (s^{-1})
k_i^0	pre-exponential factor of step i (s^{-1})
L	reactor length (m)
m_i	molecular mass (kg)
N	number of grid points
N_S	number of surface sites per unit area (m^{-2})
R	ideal gas constant (J/(mol K))
r_i	rate of step i (s^{-1})
S_{cat}	total surface area of catalyst (m^2)
s_i	sticking coefficient for adsorption step i
T	catalyst temperature (K)
T_{gas}	gas-phase temperature (K)
t	time (s)
u	axial velocity (m/s)
V	reactor volume (m^3)
P_b	partial pressure of type b species (Pa)
P_b^{in}	inlet partial pressure of type b species (Pa)
z	axial coordinate (m)
θ_a	surface coverage of type a species
θ_*	vacant site coverage
η_{CO}	conversion of CO to CO_2 (%)
η_{NO}	conversion of NO to N_2 (%)
ξ	($=z/L$) dimensionless axial coordinate
τ	residence time (s)

where (∗) denotes an empty adsorption site on a catalyst surface. When oxygen is not in excess and O_{ads} species are quickly removed from a catalyst surface via CO oxidation and/or H_2O formation reactions, then the formation of NO_{ads} is practically impossible. On the contrary, when oxygen is in excess, the formation of NO_{ads} becomes important especially at elevated temperatures.

In the previous publication [12] the kinetic model of the $NO + CO + O_2$ catalytic reaction in an isothermal continuous stirred tank reactor (CSTR) has been introduced. This model predicts a non-monotonic dependence of the NO-to-N_2 conversion on the active catalyst surface area (S_{cat}) at sufficiently high catalyst temperatures. In brief, this interesting effect has the following explanation. As S_{cat} is increasing, the partial pressure and surface coverage of CO are decreasing, but the surface oxygen coverage is progressively growing. High concentrations of adsorbed oxygen not only inhibit the NO_{ads} dissociation but also promotes the NO_{ads} formation, as a result, the NO conversion starts decreasing when S_{cat} exceeds some critical value. However, these results can only be observed at sufficiently high temperatures when the NO_{ads} formation rate becomes significant. If this reaction is not included in the reaction mechanism, the decrease in NO conversion can hardly be observed when S_{cat} becomes larger.

As discussed in Ref. [12], many unexpected phenomena have been discovered in laboratory experiments concerning the reduction of NO by CO and/or C_xH_y under strongly oxidizing conditions. Typically, the experimental results are reported in terms of "NO_x conversion" which is the fraction of NO converted to N_2 and N_2O (but not to NO_2). It was observed that a decrease of catalyst loading can result in an increase in NO_x conversion. Usually, such experimental findings are considered as evidence that the reduction of NO by CO/C_xH_y is a structure-sensitive reaction. Another example

of interesting results can be found in the work of Cho [13] who investigated the influence of the space velocity on the conversion of NO_x in the $C_3H_6 + NO + O_2$ and $C_2H_4 + NO + O_2$ reactions. He discovered that "... the NO conversion above the maximum NO-conversion temperature can be improved by increasing the space velocity rather than by decreasing it". These unusual observations, which were obtained over Cu-ZSM5 [13] and Pt-ZSM5 [14] catalysts, can hardly be attributed to a structure-sensitivity. Note that these experimental data were measured under well-controlled isothermal conditions, so they could not be caused by the additional heat generated by the chemical reactions at higher flow rates. Cho has characterized his results in the following way: "Obviously, this is contrary to the conventional physical intuition" [13]. In fact, the influence of the space velocity on the NO conversion is analogous to the influence of the catalyst surface area. As it was mentioned in Ref. [12], the stationary solutions of the isothermal CSTR model depend on a ratio F/S_{cat} only (where F is a flow rate of gas mixture which determines a space velocity). Thus, a decrease of S_{cat} has the same effect as an increase of F.

For the CSTR model, the gas- and solid-phase concentrations of all reactants, intermediates and products are assumed to be uniform inside the reactor. In this work, we extend the previous results by considering a more realistic model of a fixed-bed catalytic reactor, namely, we consider the one-dimensional axially dispersed plug flow reactor. The resulting mathematical model is constituted by a system of partial differential equations (PDEs) of the convection–diffusion–reaction type. The differential equations are obtained from conservation equations, applied separately to the gas and solid phases. This model also assumes complete mixing but only in the radial direction. Mixing in the axial direction (i.e., the direction of flow) is controlled by the diffusion/dispersion process of gaseous species in porous media. In the limit of "infinitely fast" diffusion, this model transforms to the CSTR model studied in Ref. [12]. The ideal plug flow reactor (PFR) model corresponds to zero values of the diffusion coefficients. For realistic values of (molecular) diffusion coefficients, the model is referred to as the DPFR model. In this work, we compare the predictions of these three models (CSTR, PFR and DPFR) concerning the dependence of the NO conversion on the catalyst surface area. In particular, we show that both the CSTR and DPFR models can give a non-monotonic dependence of the NO conversion on S_{cat}, whereas the ideal PFR model cannot capture this effect.

2. Mathematical model

2.1. Kinetic model

A simplified kinetic model of the catalytic $NO + CO + O_2$ reaction has been described in Ref. [12]. This model is summarized in Table 1 where the reaction mechanism, the rate constants and rate expressions are presented. The reaction mechanism comprises ten individual reaction steps, four adsorbed species (CO_{ads}, O_{ads}, NO_{ads}, N_{ads}), empty adsorption sites on the catalyst surface (∗), and five gaseous species (CO_{gas}, $O_{2,gas}$, NO_{gas}, $N_{2,gas}$, and $CO_{2,gas}$). Gas-phase reactions can be neglected at the temperatures and pressures of interest. For the sake of simplicity, the unwanted reaction by-products, N_2O and NO_2, are not considered. The kinetic scheme (R1)–(R10) represents an extension of the previously suggested scheme for the NO + CO reaction (on Rh(1 1 1) and Rh/Al_2O_3 in Ref. [5], and on Pt(1 0 0) in Ref.[7]). We added only the NO_{ads} formation reaction and the dissociative adsorption–desorption of O_2. It should be noted that we have not attempted to model concrete experimental data. Our purpose is to qualitatively describe some general characteristics inherent to the catalytic NO reduction (by

Table 1
Kinetic model of the NO + CO + O$_2$ reaction.

Step, i		k_i^0 (s^{-1})	E_i (kJ/mol)	r_i (s^{-1})
(R1) CO adsorption	CO$_{gas}$ + * → CO$_{ads}$	Eq. (1)	0	$k_1(P_{CO})\theta_*$
(R2) O$_2$ adsorption	O$_{2,gas}$ + 2* → 2O$_{ads}$	Eq. (1)	0	$k_2(P_{O_2})\theta_*^2$
(R3) NO adsorption	NO$_{gas}$ + * → NO$_{ads}$	Eq. (1)	0	$k_3(P_{NO})\theta_*$
(R4) CO desorption	CO$_{ads}$ → CO$_{gas}$ + *	10^{15}	135	$k_4\theta_{CO}$
(R5) CO$_2$ formation	CO$_{ads}$ + O$_{ads}$ → CO$_{2,gas}$ + 2*	10^{13}	90	$k_5\theta_{CO}\theta_O$
(R6) NO dissociation	NO$_{ads}$ + * → N$_{ads}$ + O$_{ads}$	10^{13}	90	$k_6\theta_{NO}\theta_*$
(R7) N$_2$ desorption	2 N$_{ads}$ → N$_{2,gas}$ + 2*	10^{12}	90	$k_7\theta_N^2$
(R8) NO desorption	NO$_{ads}$ → NO$_{gas}$ + *	10^{15}	130	$k_8\theta_{NO}$
(R9) NO formation	N$_{ads}$ + O$_{ads}$ → NO$_{ads}$ + *	10^{13}	130	$k_9\theta_O\theta_N$
(R10) O$_2$ desorption	2O$_{ads}$ → O$_{2,gas}$ + 2*	10^{13}	220	$k_{10}\theta_O^2$

CO and/or C$_x$H$_y$) under oxygen-rich conditions. The phenomena of our interest occur in a wide range of the model parameters.

The kinetic parameters presented in Table 1 were mostly taken from temperature-programmed desorption (TPD) experiments and DFT calculations for a Pt(1 0 0) surface. The rate constants for CO desorption are practically the same as those determined for Pt(1 0 0) − (1 × 1) (at θ = 0.5) [15]. The activation energy for N$_2$ desorption (E_7) was estimated from the experimental TPD spectrum of N$_2$ from Pt(1 0 0) [16], assuming that $k_7^0 = 10^{12}$ s^{-1}. For an initial coverage of 0.5 ML and a heating rate of 13 K/s, the calculated TPD spectrum has the peak position at 390 K, which coincides with the experimental value. The activation energies of the CO oxidation and NO dissociation reactions were taken from DFT calculations (Ref. [17] and Refs. [11,18], respectively), and the "normal" pre-exponential factors (10^{13} s^{-1}) were assumed.

The model assumptions concerning the N-containing reaction products are based on the following experimental observations. In Ref. [19], the catalytic reduction of NO (0.1%) with CO (1%) in the presence of excess oxygen (2%) was investigated over 7 metals supported on Al$_2$O$_3$ and over Ir and Rh supported on 6 metal oxides. It was found that Ir/WO$_3$ was the most active catalyst for the NO reduction by CO, and it showed the highest value of N$_2$ selectivity (defined as the ratio of NO converted to N$_2$ to the total conversion of NO to N$_2$ and N$_2$O) equal to 82%. However, for most other metals the selectivity for N$_2$ formation was not higher than that for N$_2$O. The N$_2$ selectivity of about 60% was found for the NO + C$_2$H$_4$ + O$_2$ reaction over Pt-ZSM-5 and Pt/Al$_2$O$_3$ catalysts [14]. On Rh/Al$_2$O$_3$ catalyst, the N$_2$ selectivity is typically close to 50% [19,20]. In these and many other experimental studies, the rates of N$_2$ and N$_2$O formation show a very similar dependence on the catalyst temperature, and the peak temperatures of N$_2$ and N$_2$O almost coincide. Thus, for simplicity, the model considers only the formation of N$_2$ via the reaction (R7). We also performed test calculations in which the formation of N$_2$O by the reaction NO$_{ads}$ + N$_{ads}$ → N$_2$O$_{gas}$ was included, but no essential changes were detected for the total conversion of NO (to N$_2$ and N$_2$O) as compared to the case when only N$_2$ is produced.

Furthermore, the formation of NO$_2$ is disregarded in the model under study, assuming that a negligible amount of NO$_2$ is formed because of kinetic limitations. For instance, Meunier et al. [21] showed that low loading (<2 wt.%) Co or Ag supported on alumina, were not significantly active for the oxidation of NO to NO$_2$ at the temperatures at which these materials were active for the SCR reaction. According to the thermodynamic equilibrium of the reaction 2NO$_{gas}$ + O$_{2,gas}$ ↔ 2NO$_{2,gas}$, the NO/NO$_2$ ratio is about 9/1 at typical temperature and pressure conditions of our interest (T = 500 °C, 1000 ppm NO, 1.6 vol.% O$_2$ in Argon). The equilibrium calculations give an upper limit for NO$_2$ formation in a continuous-flow reactor (if no other reactions are involved). Therefore, under our conditions, the amount of NO$_2$ should be small relative to NO, even if there are no kinetic limitations. Another argument in support of our assumption is that the NO$_2$ + CO + O$_2$ and NO + CO + O$_2$ reactions give very

similar results, but only if oxygen is in excess [22]. These data can be interpreted to indicate that in the oxygen-rich gas-phase, the presence of some amount of NO$_2$ (instead of NO) does not have essential influence on the NO$_x$ conversion.

Detailed modeling of N$_2$O and NO$_2$ formation greatly increases the complexity and uncertainty of the model; therefore, we restricted the model to the case of N$_2$ as the only N-containing product. This simple model describes several basic features of the catalytic NO + CO + O$_2$ reaction. Clearly, a more comprehensive model should include many other reactions and adsorbates, and it must be specific to the catalyst and support materials. However, a simple model is more helpful in understanding the basic mechanisms responsible for a particular phenomenon. The kinetic model presented in Table 1 is aimed at the study of two peculiar effects that have been observed in many experimental studies using different catalysts.

In the kinetic model, the reactions of N$_2$ and CO$_2$ formation are treated as irreversible, since it is well known that N$_2$ and CO$_2$ molecules are thermodynamically stable with respect to their elements. Substantial activation energy is required to dissociatively chemisorb these molecules on transition metal catalysts (see, e.g., DFT-based calculations for dissociative chemisorption of N$_2$ on Pt(1 0 0) [10,11], and for dissociative chemisorption of CO$_2$ on Rh(1 1 1) [23]). The activation of N$_2$ in the high-frequency discharge is required to adsorb atomic nitrogen on Pt single crystals [16]. The chemical reactivity of CO$_2$ can be expected if H-containing species are involved in the reaction mechanism [24], but such species are not considered here.

In this work the kinetic model is studied under non-equilibrium conditions. Nevertheless, the overall thermodynamic consistency of the model can be tested by comparing the steady-state conversions of NO and CO in an isolated system with that predicted by the thermodynamic equilibrium. To calculate the thermodynamic equilibrium composition, we consider the following set of gas-phase reactions:

$$2NO \leftrightarrow O_2 + N_2,$$

$$2CO + O_2 \leftrightarrow 2CO_2,$$

$$2NO + O_2 \leftrightarrow 2NO_2,$$

$$3NO \leftrightarrow N_2O + NO_2$$
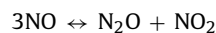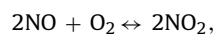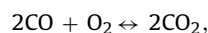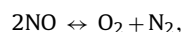
The typical temperature and pressure conditions used in this study are: T = 773 K, a total pressure of 1 atm, the partial pressures P_{NO} = 0.001 atm, P_{CO} = 0.0075 atm, P_{O_2} = 0.02 atm. Under these conditions, the following equilibrium partial pressures [atm] can be calculated: $P_{O_2}^{eq} \approx 0.01675$; $P_{N_2}^{eq} \approx 5 \times 10^{-4}$; $P_{NO}^{eq} \approx 10^{-8}$; $P_{CO}^{eq} \approx 10^{-16}$; $P_{NO_2}^{eq} \approx 10^{-9}$; $P_{N_2O}^{eq} \approx 2 \times 10^{-14}$. Thus, the equilibrium calculations predict that NO conversion to N$_2$ is 99.999%, CO conversion to CO$_2$ is practically 100%, while the amounts of N$_2$O and NO$_2$ are

negligibly small. For an isolated system at equilibrium, the kinetic model gives essentially the same results: the conversion efficiency of NO and CO is 100%, because the reaction products are formed by the irreversible reactions. Of course, this conclusion is valid only under the conditions adopted in the present study (at temperatures below 1000 K and at relatively low partial pressures of reactants). A very low content of NO (0.01 ppm) in the equilibrium composition is due to the fact that NO has a positive standard free energy of formation, so that the direct NO decomposition reaction is thermodynamically favored at ambient and up to relatively high temperatures [25]. However, it has proven difficult to find a catalyst that is active for direct NO decomposition in the presence of oxygen.

In the model equations, the surface concentrations of adsorbed species are denoted as θ_a. Here and below, the subscript "a" designates different species on the catalyst surface: $a = \{CO, O, NO, N\}$. The concentration of empty surface sites, θ_*, is calculated as: $\theta_* = 1 - \sum_a \theta_a$. The partial pressures of reactants in the gas phase are denoted as P_b. Here and below, the subscript "b" designates different species in the gas-phase: $b = \{CO, O_2, NO\}$.

The rates of surface reactions, r_i ($i = 1, \ldots, 10$) [s^{-1}], are determined by the mass action law. The rate constants k_i are calculated using the Arrhenius equation:

$$k_i = k_i^0 \exp\left(-\frac{E_i}{RT}\right),$$

where k_i^0 [s^{-1}] is the pre-exponential factor, E_i [J/mol] is the activation energy, T [K] is the catalyst temperature, R [J/(mol K)] is the ideal gas constant. Each prefactor for the adsorption process, k_i^0 ($i = 1, 2, 3$), is linearly dependent on the appropriate partial pressure; it is calculated from the kinetic theory of gases using the following equation:

$$k_i^0(P_i) = P_i s_i (2\pi m_i k_B T_{gas})^{-0.5} (N_S)^{-1} \tag{1}$$

where P_i [Pa] is the partial pressure, s_i is the sticking coefficient, m_i [kg] is the molecular mass, k_B [J/K] is the Boltzmann constant, T_{gas} [K] is the gas temperature, N_S [m^{-2}] is the number of surface sites per unit area. To calculate the adsorption rates, we used the following values: $N_S = 10^{19}$ m^{-2}, $T_{gas} = 300$ K, $s_1 = s_2 = s_3 = 0.1$.

The following kinetic equations describe the mass balance on the catalyst surface:

$$\frac{d\theta_{CO}}{dt} = r_1 - r_4 - r_5 \equiv f_{CO},$$

$$\frac{d\theta_O}{dt} = 2r_2 - r_5 + r_6 - r_9 - 2r_{10} \equiv f_O,$$

$$\frac{d\theta_{NO}}{dt} = r_3 - r_6 - r_8 + r_9 \equiv f_{NO}, \tag{2}$$

$$\frac{d\theta_N}{dt} = r_6 - 2r_7 - r_9 \equiv f_N.$$

2.2. Model of a fixed-bed catalytic reactor

In Ref. [12] the kinetic model (2) has been studied under isothermal CSTR conditions. The heat balance is not considered in this study, because the high thermal conductivity of the catalyst bed, quite low concentrations of reactants in the feed mixture, and effective temperature control of a small-scale reactor are assumed. The isothermicity of the catalyst bed is usually well satisfied in laboratory experiments for kinetic studies; for example, in Ref. [14] it was shown that the effect of reaction exotherm on the observed reaction rate was negligible.

For the CSTR model, the gas- and solid-phase concentrations of all reactants, intermediates and products are assumed to be uniform inside the catalytic reactor. Now we consider a more general

and more realistic mathematical model, namely, the axially dispersed plug-flow reactor model. This model, abbreviated as DPFR, also assumes complete mixing but only in the radial direction. Mixing in the axial direction is controlled by the diffusion (dispersion) process of gaseous species in porous media. Therefore, the partial pressures P_b and the surface coverages θ_a now depend on the axial coordinate z. Eq. (2) gives the kinetic model at any "point" which is at a distance z from the reactor inlet, and it can be rewritten as:

$$\frac{\partial \theta_a(z, t)}{\partial t} = f_a(\boldsymbol{\theta}(z, t), \mathbf{P}(z, t)) \tag{3}$$

where $\boldsymbol{\theta} = (\theta_{CO}, \theta_O, \theta_{NO}, \theta_N)$, $\mathbf{P} = (P_{CO}, P_{O_2}, P_{NO})$; $z \in (0, L)$, L [m] is the reactor length. The DPFR model is used to describe non-ideal chemical reactors, where the axial dispersion is superimposed on the plug flow of an ideal gas. The model is based on the following one-dimensional convection–diffusion–reaction equation:

$$\frac{\partial P_b(z, t)}{\partial t} = -u \frac{\partial P_b(z, t)}{\partial z} + D_b \frac{\partial^2 P_b(z, t)}{\partial z^2} - W_b(\boldsymbol{\theta}(z, t), \mathbf{P}(z, t)), \tag{4}$$

where u [m/s] is the superficial gas velocity, D_b [m^2 s^{-1}] are the diffusion (dispersion) coefficients. The reaction terms, W_b, are given by the difference between the adsorption and desorption fluxes: $W_{CO} = \sigma(r_1 - r_4)$, $W_{O2} = \sigma(r_2 - r_{10})$, $W_{NO} = \sigma(r_3 - r_8)$. The coefficient σ [Pa] is calculated from the formula: $\sigma = N_S k_B T_{gas} S_{cat} V^{-1}$, where V [m^3] is the reactor volume, S_{cat} [m^2] is the total surface area of catalyst, which is homogeneously distributed throughout the reactor. The gas and catalyst temperatures are assumed to be constant.

The convection–diffusion–reaction Eq. (4) is supplemented by a Robin-type boundary condition at the inflow boundary and a Neumann-type boundary condition at the outflow boundary (also known as "Danckwerts' boundary conditions"):

$$z = 0 : u(P_b - P_b^{in}) = D_b \frac{\partial P_b}{\partial z};$$

$$z = L : \frac{\partial P_b}{\partial z} = 0; \tag{5}$$

where P_b^{in} is the inlet partial pressure. The physical implication of the Danckwerts boundary conditions is that the dispersive flux across the reactor boundaries is zero.

The system (3)–(5), with specific initial conditions, represents the DPFR model. It is important to mention that the DPFR model reduces to the PFR and the CSTR models in the limits of $D_b = 0$ and $D_b \to \infty$ (for all b), respectively.

2.3. Numerical methods

In this study only the stationary solutions of Eqs. (3)–(5) will be considered. The steady state model equations are obtained by equating the time derivatives in Eqs. (3) and (4) to zero, which reduces them to a set of ordinary differential equations in the spatial coordinate. For further considerations it is convenient to change the axial coordinate z ($0 \leq z \leq L$) with the dimensionless coordinate $\xi = z/L$ ($0 \leq \xi \leq 1$). The resulting equations for the stationary solutions are given below:

$$f_a(\boldsymbol{\theta}, \mathbf{P}) = 0, \tag{6}$$

$$\bar{D}_b \frac{d^2 P_b}{d\xi^2} - \frac{1}{\tau} \frac{dP_b}{d\xi} - W_b(\boldsymbol{\theta}, \mathbf{P}) = 0, \tag{7}$$

$$\frac{1}{\tau}(P_b - P_b^{in})\Big|_{\xi=0} = \bar{D}_b \frac{dP_b}{d\xi}\Big|_{\xi=0},$$

$$\frac{dP_b}{d\xi}\Big|_{\xi=1} = 0, \tag{8}$$

where τ [s] is the residence time, $\tau = V/F = L/u$; F [m^3 s^{-1}] is the volumetric flow rate; $\bar{D}_b = D_b/L^2$ [s^{-1}].

For numerical solution of Eqs. (6)–(8) we used a one-dimensional uniform grid $\{\xi_n = h(n-0.5); \ h = N^{-1}; \ n = 1, \ldots, N\}$, where N is the number of grid points, h is the grid spacing. The continuous functions $\theta_a(\xi)$ and $P_b(\xi)$ are defined at the grid points ξ_n as $\theta_{a,n} = \theta_a(\xi_n)$ and $P_{b,n} = P_b(\xi_n)$, respectively. Applying finite-difference approximations to the partial derivatives appearing in Eq. (7) at the grid points ξ_n yields,

$$\frac{\bar{D}_b}{h^2}(P_{b,n-1} - 2P_{b,n} + P_{b,n+1}) + \frac{1}{h\tau}(P_{b,n-1} - P_{b,n})$$
$$-W_b(\boldsymbol{\theta}_n, \mathbf{P}_n) = 0. \tag{9}$$

The values of $P_{b,0}$ and $P_{b,N+1}$ remain to be determined. The quantity $P_{b,0}$ can be determined from a finite-difference approximation of the boundary condition at $\xi = 0$:

$$\frac{1}{\tau}(P_{b,0} - P_b^{in}) = \bar{D}_b \frac{P_{b,1} - P_{b,0}}{h}.$$

To implement the boundary condition at $\xi = 1$, we assume that $P_{b,N+1} = P_{b,N}$. Then we arrive at the following algebraic system:

$$f_a(\boldsymbol{\theta}_n, \mathbf{P}_n) = 0, \quad (n = 1, 2, \ldots, N), \tag{10.1}$$

$$\frac{\bar{D}_b}{h^2}(P_{b,2} - P_{b,1}) + \frac{1}{h\tau}(P_b^{in} - P_{b,1}) - W_b(\boldsymbol{\theta}_1, \mathbf{P}_1) = 0, \tag{10.2}$$

$$\frac{\bar{D}_b}{h^2}(P_{b,n-1} - 2P_{b,n} + P_{b,n+1}) + \frac{1}{h\tau}(P_{b,n-1} - P_{b,n})$$
$$-W_b(\boldsymbol{\theta}_n, \mathbf{P}_n) = 0, \quad (n = 2, \ldots, N-1), \tag{10.3}$$

$$\frac{\bar{D}_b}{h^2}(P_{b,N-1} - P_{b,N}) + \frac{1}{h\tau}(P_{b,N-1} - P_{b,N}) - W_b(\boldsymbol{\theta}_N, \mathbf{P}_N) = 0. \tag{10.4}$$

Eq. (10) constitutes a closed system for the determination of $7N$ unknowns, $\theta_{a,n}$ and $P_{b,n}$. All simulation results presented in this study were calculated from Eq. (10). Note that at $\bar{D}_b = 0$ the system (10) gives a first-order upwind scheme for the ideal PFR model. Formally, the CSTR model follows from Eqs. (10.1) and (10.2) if $N = 1$ and $\bar{D}_b = 0$. In numerical simulations the CSTR solution will be attained for any finite value of L when $\bar{D}_b \to \infty$ for all b. Moreover, Eq. (10) gives a model known as a "cascade of isothermal CSTRs" which, in fact, is equivalent to the finite-difference approximation of the ideal PFR model (at $\bar{D}_b = 0$).

For the calculations, we used the same parameter values as in Ref. [12], that is: $N_s = 10^{19} \ m^{-2}$, $T_{gas} = 300 \ K$, $F = 2 \times 10^{-6} \ m^3 \ s^{-1}$, $P_{CO}^{in} = 7.5 \times 10^2 \ Pa$, $P_{O_2}^{in} = 2 \times 10^3 \ Pa$, $P_{NO}^{in} = 10^2 \ Pa$. The additional parameters involved in the DPFR model are the reactor length (L), the reactor volume (V), and the diffusion coefficients (D_b). Note that the steady states of the CSTR and PFR models are independent on these parameters. In accordance with laboratory experiments in a small-scale reactor, the following values are employed for the computations: $L = 10^{-2} \ m$, $V = 10^{-6} \ m^3$. For simplicity, it is assumed that the dispersion coefficients of all species are equal to each other and correspond to the molecular diffusion coefficients (at standard conditions): $D = D_{CO} = D_{O_2} = D_{NO} = 2 \times 10^{-5} \ m^2 s^{-1}$. Thus, the steady states of the DPFR model depend on the only additional parameter DVL^{-2}.

The main quantities of interest, which characterize the catalytic reactor performance, are the CO-to-CO_2 and NO-to-N_2 conversions. These values, denoted as η_{CO} and η_{NO}, are calculated as follows:

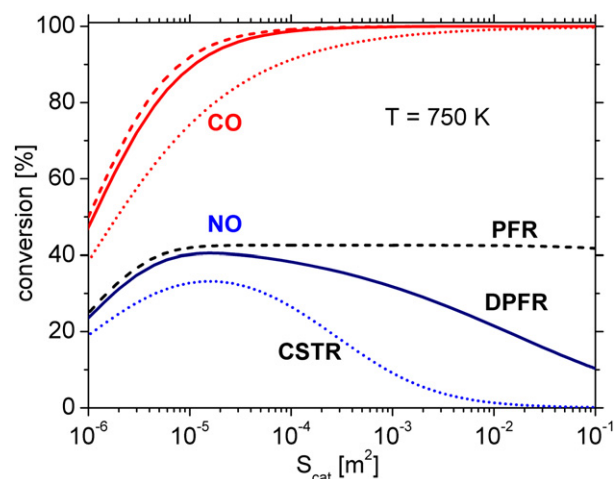$$\eta_{CO} = \left(\frac{P_{CO}^{in} - P_{CO,N}}{P_{CO}^{in}}\right) \times 100\%,$$

Fig. 1. Steady-state conversions of NO and CO as the functions of S_{cat} at $T = 750$ K. The simulation results for the CSTR, PFR and DPFR models are presented.

$$\eta_{NO} = \left(\frac{P_{NO}^{in} - P_{NO,N}}{P_{NO}^{in}}\right) \times 100\%.$$

In order to discretize the first-order spatial derivative term in Eq. (4) taking into account the boundary conditions (5), various numerical approximations can be proposed. The finite-difference scheme (10) represents the first-order upwind scheme, perhaps it is the simplest approximation. To check our results, we have also implemented the second-order central finite-difference scheme. We have compared these numerical approximations of Eqs. (3)–(5) on several test examples. However, no essential differences between the calculated solutions were revealed, presumably because we used rather fine grids at rather low space velocity.

The steady states were calculated with the help of a numerical continuation procedure using the pseudo-arclength continuation algorithm [26]. The catalyst surface area, S_{cat}, and temperature, T, were taken as the bifurcation parameters. When the system size was not too large (e.g., less than 10^3 equations) we applied the standard Newton's method to solve the system of $7N+1$ nonlinear algebraic equations, as required for the pseudo-arclength continuation algorithm. The Newton's method, however, entails the calculation and factorization of the Jacobian matrix, which renders the approach computationally infeasible for large problems. For the PFR and DPFR models we also applied very fine grids, therefore, in this case we implemented the numerical algorithm based on a matrix-free Newton–Krylov method. This algorithm is described in details in Ref. [27]. The matrix-free approach allowed us to perform a one-parameter continuation for very large systems (of up to 10^6 equations) in reasonable time.

3. Simulation results and discussion

The steady-state conversions of CO and NO as the functions of S_{cat} for the CSTR, PFR and DPFR models are compared in Fig. 1. When S_{cat} is increasing, all three models show similar behavior with respect to the CO conversion. At large values of S_{cat}, the value of η_{CO} approaches 100%. However, these models give markedly different results for the NO conversion. The CSTR and DPFR models do show the non-monotonic dependencies of η_{NO} on S_{cat}, whereas the PFR model does not show such effect. For the PFR model, the NO conversion decreases only slightly at large values of S_{cat}, but this result is caused by insufficient numerical accuracy, as will be discussed below. The three models are distinguished by the single parameter $D : D \to \infty$ (for CSTR), $D = 0$ (for PFR), $D = 0.2 \ cm^2 \ s^{-1}$ (for
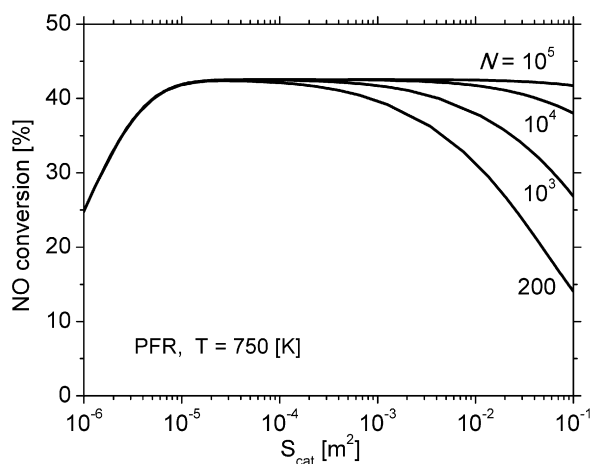
Fig. 2. Influence of the grid size on the solution of the PFR model. The NO-to-N$_2$ conversions versus S_{cat} at $T=750$ K are shown for different numbers of grid points N.

DPFR). Therefore, the gas phase diffusion of reactants is required to obtain the non-monotonic dependence of η_{NO} on S_{cat}. This interesting effect is the most pronounced for the CSTR model, when diffusion is infinitely fast. When diffusion is absent, the quantity η_{NO} almost approaches a maximum value already at $S_{cat} \approx 10^{-5}$ m^2, and further increase of S_{cat} does not change η_{NO} significantly.

For the PFR model, Fig. 2 displays η_{NO} calculated for various number of the grid points N. When accuracy is low (N is small), the spurious non-monotonic dependence of η_{NO} on S_{cat} is observed. In fact, each grid point corresponds to the center of an elementary volume in which a homogeneous distribution of all variables is assumed. Therefore, a coarse spatial discretization gives rise to

"numerical diffusion", which "creates" a spurious homogeneity. Of course, this effect is more pronounced when N is small. The incorrect solution of the PFR model (with "numerical diffusion") can become similar to the correct solution of the DPFR model (with chemical diffusion).

The results for the PFR model presented in Fig. 1 were calculated with $N=10^5$ but even this large number is insufficient to provide the accurate results. At large S_{cat} values, a very fine grid at the left boundary is required in order to calculate the correct solution to the PFR model. For $S_{cat}=10^{-1}$ m^2, Fig. 3 demonstrates the solution near the left boundary. The partial pressures P_{CO}, P_{NO}, and the oxygen coverage θ_O are shown as the functions of the normalized axial coordinate ξ. Note that $\xi=1$ correspond to the reactor outlet, so that Fig. 3 gives the solution near the reactor entrance. From Fig. 3(b) (results for $N=10^5$) one can see that a significant NO reduction occurs only at $\xi < 2 \times 10^{-4}$. When P_{CO} drops below a certain level, the conversion of NO to N$_2$ vanishes because the catalyst surface becomes inhibited by adsorbed oxygen. At $T=750$ K, the CO oxidation rate is very high ($k_5 \approx 5 \times 10^6$ s^{-1}), therefore, a relatively small amount of active catalytic sites are sufficient to give a complete conversion of CO to CO$_2$, taking into account the adopted gas feed rate and the inlet partial pressures of reactants. At high temperatures, the adsorption of CO is the rate limiting reaction for the CO oxidation reaction. Direct decomposition of NO to N$_2$ and O$_2$ is hardly possible because at this temperature the oxygen desorption is very slow. That is why only a very small portion, about 0.001%, of the reactor volume is active, whereas the remaining portion is completely inactive because it is poisoned by atomic oxygen. The data presented in Fig. 3 also demonstrate that the grids with $N < 10^5$ cannot give the correct results with respect to η_{NO}. On the contrary, a correct value of η_{CO} (close to 100%) can be calculated by using a very coarse grid. It should be mentioned that the amount of the grid points required to calculate the correct
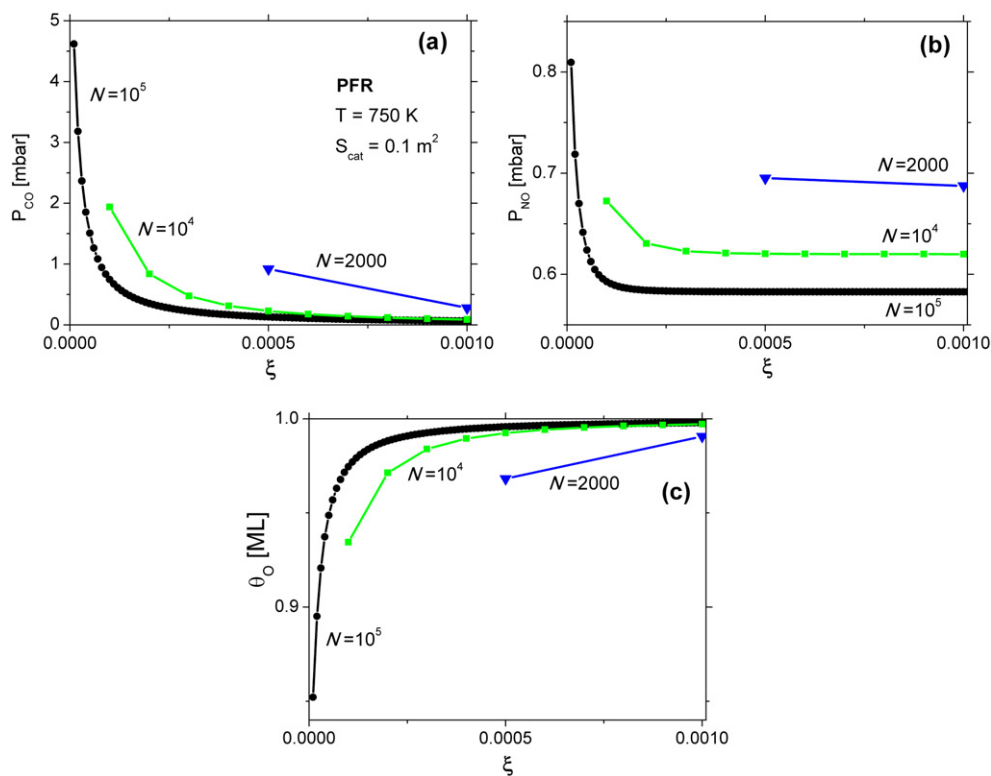

Fig. 3. Steady-state solutions of the PFR model near the reactor inlet for different numbers of grid points: $N=2 \times 10^3$ (blue triangles), $N=10^4$ (green squares), and $N=10^5$ (black circles). Shown are the profiles of (a) the partial pressure of CO, (b) the partial pressure of NO, (c) the adsorbed oxygen concentration. The results were calculated for $T=750$ K, $S_{cat}=0.1$ m^2. (For interpretation of the references to color in this figure legend, the reader is referred to the web version of the article.)
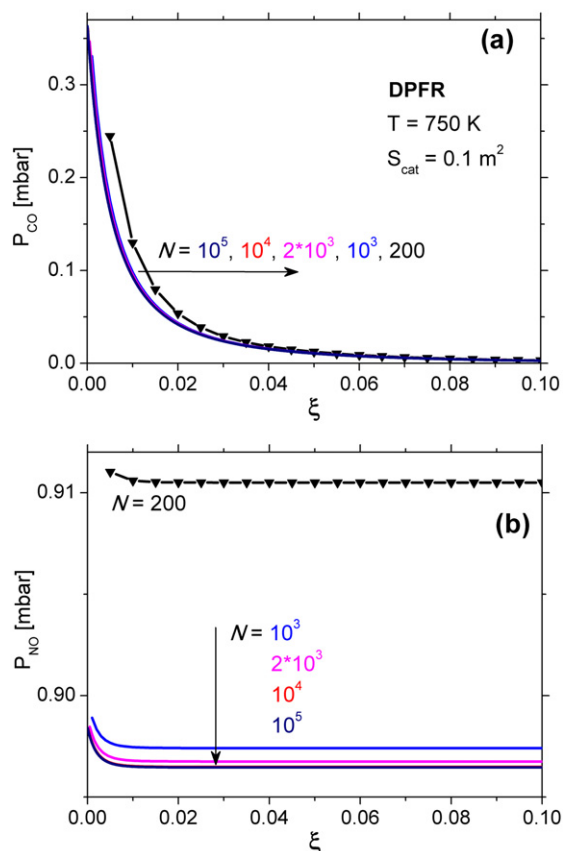
Fig. 4. Steady-state solutions of the DPFR model near the reactor inlet for different numbers of grid points. Shown are the profiles of (a) the partial pressure of CO, (b) the partial pressure of NO. The results were calculated for $T = 750$ K, $S_{cat} = 0.1$ m^2.

Fig. 5. Steady-state solutions of the DPFR model (using $N = 2 \times 10^3$) for different values of S_{cat} : 10^{-4} m^2 (black curve), 10^{-3} m^2 (blue), 10^{-2} m^2 (magenta). Shown are the profiles of (a) the partial pressure of CO, (b) the partial pressure of NO. The results were calculated at $T = 750$ K. (For interpretation of the references to color in this figure legend, the reader is referred to the web version of the article.)

η_{NO} can be significantly reduced by using a non-uniform grid which is finer near the reactor inlet.

The accurate solution of the DPFR model can be calculated using a relatively coarse grid, e.g., a value of $N = 2 \times 10^3$ already gives satisfactory results, as demonstrated in Fig. 4. In the presence of chemical diffusion, the role of "numerical diffusion" diminishes. Fig. 4(a) shows that P_{CO} drops to almost zero at a much larger value of ξ (≈ 0.1) as compared to that for the PFR model ($\xi \approx 0.001$). Partial pressures undergo discontinuity at the domain entrance, because of the Danckwerts boundary conditions and the significant diffusion of gas-phase species. Remarkably, P_{CO} near the left boundary is much lower than that for the PFR model. Since the adsorption of CO is the rate-limiting step, the reaction occurs near the reactor inlet much more slowly as compared with a case where diffusion is absent. Unlike that for the PFR model, the partial pressure of NO exceeds the partial pressure of CO at each point in the reactor (cf. Fig. 4(a) and (b)). Under the steady-state conditions, conversion of NO to N$_2$ can take place only when there is a significant amount of CO in the gas phase because, otherwise, the whole surface becomes poisoned by atomic oxygen. It is important to point out that we consider the catalytic reaction under conditions where oxygen is in large excess.

The influence of the CO partial pressure on the NO conversion is further demonstrated in Fig. 5, where the partial pressures P_{CO} and P_{NO} are shown as the functions of the normalized axial coordinate ξ for several fixed values of S_{cat}. Fig. 5(a) shows that the values of $P_{CO}(\xi)$ at $S_{cat} = 10^{-4}$ m^2 are much larger than those at $S_{cat} = 10^{-2}$ m^2. However, near the reactor outlet (at $\xi = 1$, not shown) they both are close to zero, so that the CO conversion is nearly
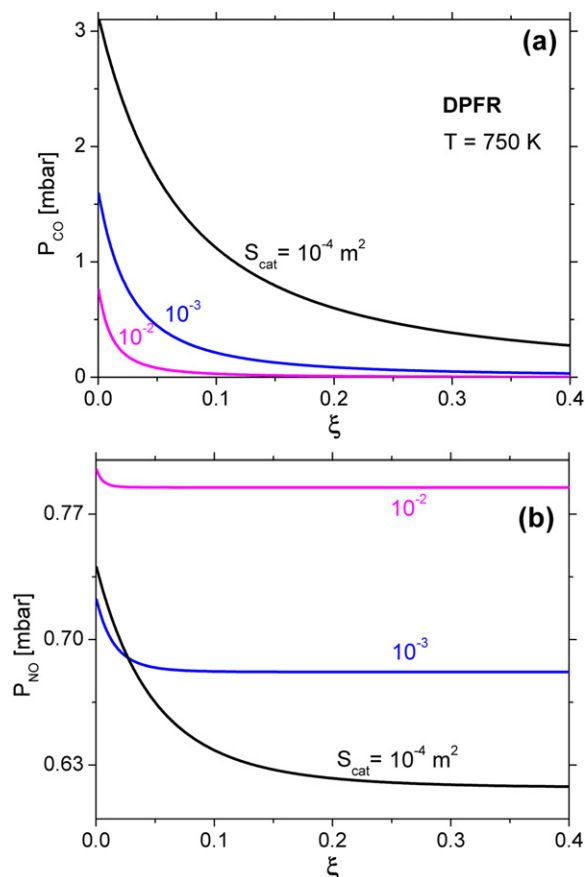
100%. The corresponding values of $P_{NO}(\xi)$ (see Fig. 5(b)) confirm that the catalyst with smaller surface area exhibits better conversion of NO than the catalyst with larger surface area. A reasonable explanation for this effect is based on the influence of P_{CO} on the NO conversion efficiency. A large catalyst surface area can be detrimental with respect to the NO conversion, because the insufficient amount of the reductant (CO) causes ineffective reduction of the oxidant NO. These explanations, however, do not provide a clear understanding of why the non-monotonic dependence of η_{NO} on S_{cat} can only be observed when the reaction of NO formation (R9) is included in the reaction mechanism. If we set $k_9 = 0$, then the calculated $P_{CO}(\xi)$ is practically identical to that shown in Fig. 5(a), but the calculated $P_{NO}(\xi)$ is quite opposite to that shown in Fig. 5(b). In this case, the "normal" dependency of η_{NO} on S_{cat} is observed – a larger surface area leads to higher, not lower, efficiency of the NO reduction.

The influence of catalyst temperature on the reactor efficiency is demonstrated in Fig. 6. The steady-state conversions of CO and NO as the functions of S_{cat} at different temperatures are presented in Fig. 6(a). In the temperature range of interest, the functions $\eta_{CO}(S_{cat})$ are practically independent on T, and the four red curves almost coincide with each other. Quite the contrary, the functions $\eta_{NO}(S_{cat})$ are strongly temperature-dependent. In particular, with decreasing T, the non-monotonic dependence of η_{NO} on S_{cat} becomes less pronounced, and it completely disappears at even lower T.
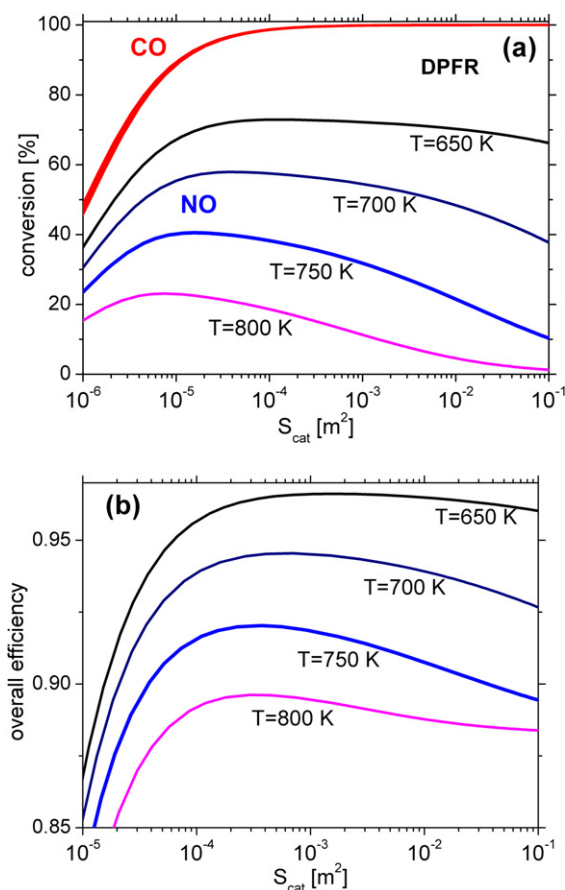
Fig. 6. (a) Steady-state conversions of CO and NO as the functions of S_{cat} for the DPFR model. The NO conversions are shown at different temperatures: $T = 650\,K$ (black curve), $T = 700\,K$ (navy), $T = 750\,K$ (blue), $T = 800\,K$ (magenta). The corresponding values of the CO conversions (red curves) almost coincide with each other at all temperatures. (b) The overall efficiency at different temperatures. (For interpretation of the references to color in this figure legend, the reader is referred to the web version of the article.)

The overall reactor efficiency can be defined as:

$$\eta = \frac{(P_{CO}^{in} - P_{CO,N}) + (P_{NO}^{in} - P_{NO,N})}{P_{CO}^{in} + P_{NO}^{in}}$$

This quantity is proportional to the number of molecules of the reactants, CO and NO, that are converted to the reaction products, CO_2 and N_2. The values of $\eta(S_{cat})$ calculated at different temperatures are plotted in Fig. 6(b). At $T = 750\,K$ (blue curve), one can see a significant decrease in the overall reactor efficiency with increasing S_{cat}. Both for the CSTR and DPFR models, the function $\eta(S_{cat})$ exhibits a local maximum at intermediate values of S_{cat}. When the CO conversion is almost complete, an increase in NO conversion can be induced by a decrease, not an increase, in the active catalytic surface area. Due to such a decrease in S_{cat}, the CO conversion reduces only slightly and it remains to be about 100%, but the NO conversion can be improved significantly.

Fig. 6 shows the steady-state conversions of CO and NO at relatively high temperatures. At such conditions, the DPFR model has a unique stable steady-state. At lower temperatures, however, the system may have multiple steady-states. For the lumped CSTR model, there are three steady-states, two of which are stable [12]. The space-dependent DPFR model gives much more complex results, it can have of up to $2N + 1$ stationary solutions, $N + 1$ of which are stable. Fig. 7 displays the conversion of CO (Fig. 7(a)) and NO

(Fig. 7(b)) as a function of catalyst temperature at a fixed value of $S_{cat} = 0.01\,m^2$ for $N = 100$. Solid lines denote asymptotically stable solutions and dashed lines denote unstable solutions. Fig. 7(c) shows a magnification of Fig. 7(b) in the region where multiple branches of stationary solutions are found. In essence, Fig. 7 represents a one-parameter bifurcation diagram for the DPFR model; it is constructed through numerical continuation of steady-state solutions. There are $2N$ saddle-node bifurcations (also known as turning points) where the steady-states change their stability.

At low temperatures, the catalyst's surface is predominantly covered by adsorbed CO which inhibits dissociative oxygen adsorption and keeps the catalytic rate low. A reactive state is attained at higher temperatures, when the catalytic surface is oxygen-covered and CO_2 is formed at high rate. With increasing temperature, a transition from low to high activity state takes place. This transition is related to catalytic ignition; it is initiated near the reactor inlet. The region of multistability just corresponds to a transition from a CO-covered to an O-covered state. Using an isothermal PFR-type model, similar results concerning multistability were reported for the CO oxidation reaction, and it was suggested that "an infinite number of steady states" exists [28]. Physically, multistability means that ignition of the catalytic surface can occur at any axial position in the reactor. On the other hand, the presence of $2N + 1$ steady states can be considered as an artifact of discrete numerical approximation, or as a shortcoming of the physical-chemical model. For the continuous PDE model (4), it can also be suggested that an infinite number of steady states does exist, but such a statement requires a mathematical proof. Nevertheless, a detailed investigation of the multiple steady states is not the subject of our study. Our goal is to calculate the dependencies $\eta_{NO}(T)$ for qualitative comparison with typical experimental data concerning the catalytic reduction of NO under lean-burn conditions. If the continuation algorithm is used with large values of N, then it is computationally infeasible to calculate all the steady state branches in the region of multistabilty. To overcome this problem, we defined two points denoted as A and B in Fig. 7. To calculate the dependencies $\eta_{CO}(T)$ and $\eta_{NO}(T)$ at large values of N, we used the following procedure. First, we applied the continuation algorithm in direction of increasing the bifurcation parameter (T), starting from a low value (e.g., 450 K), until the bifurcation point A is attained. Then, we applied the continuation algorithm in direction of decreasing the bifurcation parameter, starting from a high value (e.g., 900 K), until the point B is attained. In this way, we calculated only the stable steady states. The simulation results presented in the following figures were obtained using this procedure.

For the DPFR model with $N = 2000$, the graphs of $\eta_{CO}(T)$ and $\eta_{NO}(T)$ for several values of S_{cat} are displayed in Fig. 8. A transition from the bifurcation point A to the high reactivity state is shown in Fig. 8(a) by a dashed line (note that these lines are not the steady-state solutions). These simulations correspond to an experimental setup in which the steady-states conversions are measured using a gradual increase of temperature in small steps. The results shown in Fig. 8 are similar to those presented in Ref. [12] for the CSTR model. In Fig. 8 one can see that the temperature, where the NO conversion is at maximum, almost coincides with the temperature, where the CO conversion is almost complete. If S_{cat} decreases, the peak activity moves to higher temperature but the maximum of the NO conversion decreases too. Qualitatively similar results were measured, for example, over Pt/Al_2O_3 catalysts for different Pt loadings [6].

Fig. 8 shows that at low temperatures the catalyst with larger S_{cat} is more efficient than the catalyst with smaller S_{cat}, in particular, in this case a catalytic ignition ("light-off") occurs at lower temperature. At temperatures above ~600 K, however, the catalyst with small S_{cat} gives better conversion of NO than the catalyst with large S_{cat}. In both cases, the CO conversion approaches nearly 100%.
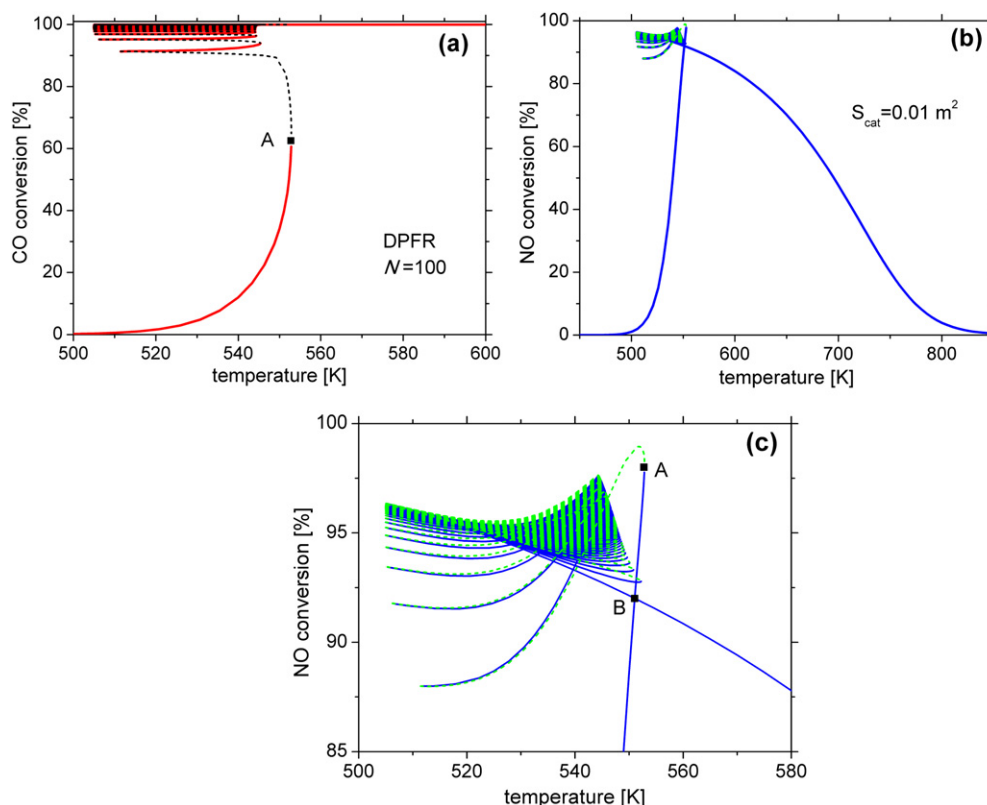
Fig. 7. Bifurcation diagrams showing the steady-state conversion of (a) CO and (b) NO as the function of temperature. Solid lines denote stable solutions, dashed lines denote unstable solutions. Panel (c) shows a magnification of Panel (b) in the region where the multiple steady-state branches coexist. The results were calculated using the DPFR model, $N = 100$, $S_{cat} = 0.1 \, \mathrm{m}^2$.

Thus, the DPFR model predicts that a decrease of catalyst loading in some cases can improve the overall reactor performance. Another "paradox", which follows from our results, is that an inert material, which blocks the active catalytic sites, can be interpreted as a catalytic promoter.

Interesting experimental results were reported in the works of Cho [13,14] who investigated the influence of the space velocity on the conversion of NO in the $C_3H_6 + NO + O_2$ and $C_2H_4 + NO + O_2$ reactions over Cu-ZSM5 [13] and Pt-ZSM5 [14] catalysts under isothermal steady-state operating conditions. He discovered that the NO conversion at high temperatures can be improved by increasing the space velocity rather than by decreasing it. Similar results can be calculated using both the CSTR and DPFR models. The steady states of the CSTR model depend on a ratio F/S_{cat} only [12]. Therefore, a decrease of S_{cat} has the same effect as an increase of F. For the DPFR model, the dependence of the steady states on the values of F and S_{cat} is not so simple, but the simulation results presented in Fig. 9 show that an increase of F has similar effect as a decrease of S_{cat} (cf. Fig. 8(b)). For $F = 2 \times 10^{-5} \, \mathrm{m}^3 \, \mathrm{s}^{-1}$ (blue curve in Fig. 9), the amount of NO molecules entering the reactor is an order of magnitude larger than that for $F = 2 \times 10^{-6} \, \mathrm{m}^3 \, \mathrm{s}^{-1}$ (black curve). Surprisingly, however, at high temperatures the conversion is larger for a larger flow rate. Thus, the DPFR model predicts the non-monotonic dependence of η_{NO} not only on S_{cat}, but on F too. This effect can only be observed at sufficiently high temperatures, when the NO$_{ads}$ formation rate is not too small.

The experimental studies of ammonia oxidation indicate that the NO$_{ads}$ formation reaction on Pt single crystal surfaces occurs even at low temperatures. For example, reflection absorption infrared spectroscopy (RAIRS) experiments [29] showed that the NO$_{ads}$ formation on Pt(1 0 0) started at around 275 K. Weststrate et al. [30], using X-ray photoelectron spectroscopy (XPS), detected

the NO$_{ads}$ formation already at 200 K on Pt(4 1 0). They also showed that for the steady-state ammonia oxidation reaction with NH$_3$/O$_2$ ratio of 1:5, N$_2$ and H$_2$O were the major products at low temperatures, whereas the selectivity toward NO and H$_2$O changed at $T > 450$ K. This temperature is determined by the desorption rates of N$_2$ and NO, rather than by the NO$_{ads}$ formation rate. These experimental studies, however, did not provide evidence that NO$_{ads}$ was formed directly from atomic nitrogen and oxygen, because NH$_x$ species were also present on the catalyst surface.

Unfortunately, the rate constant (k_9) for the NO$_{ads}$ formation step is largely unknown. Obviously, the influence of the NO$_{ads}$ formation reaction on the simulation results is also determined by the rate of the reverse reaction (the NO$_{ads}$ dissociation), the rate constant of which is largely unknown too. For the NO$_{ads}$ formation reaction, we assume a quite large activation energy (E_9) of 130 kJ/mol, so that the value of r_9 can be important only at temperatures above 600 K. For Pt-based catalysts, some of the literature data are listed below as the pairs ($k_9^0 \, [\mathrm{s}^{-1}]$, $E_9 \, [\mathrm{kJ/mol}]$) of prefactor and activation energy: $(2 \times 10^{15}, 96)$ in Ref. [9]; $(10^{13}, 128.1 - 45\theta_O)$ in Ref. [31]; $(2.1 \times 10^{13}, 131)$ in Ref. [32]; $(5.65 \times 10^{12}, 121)$ in Ref. [33]; $(5 \times 10^{14}, 88)$ in Ref. [34]; $(2.0 \times 10^{15}, 100)$ in Ref. [35]; $(2.8 \times 10^{13}, 126)$ in Ref. [36]. Thus, according to the literature data, the activation energy for the NO$_{ads}$ formation reaction varies from 88 to 131 kJ/mol. In addition, the surprisingly low activation energy, namely, 21 kJ/mol, was found for the NO$_{ads}$ formation reaction on a Pt(1 0 0) surface by means of DFT calculations [10].

It is interesting to study the sensitivity of the NO conversion efficiency to variations of the rate constant k_9. For the DPFR model, Fig. 10(a) gives the graphs of $\eta_{NO}(T)$ for $E_9 = 110$ kJ/mol, and Fig. 10(b) gives the graphs of $\eta_{NO}(T)$ for $k_9 = 0$ (i.e., for $E_9 \to \infty$). All other parameters are the same as before. Shown are the results for two values of S_{cat}. By comparing Figs. 8(b) and 10(a), it can be
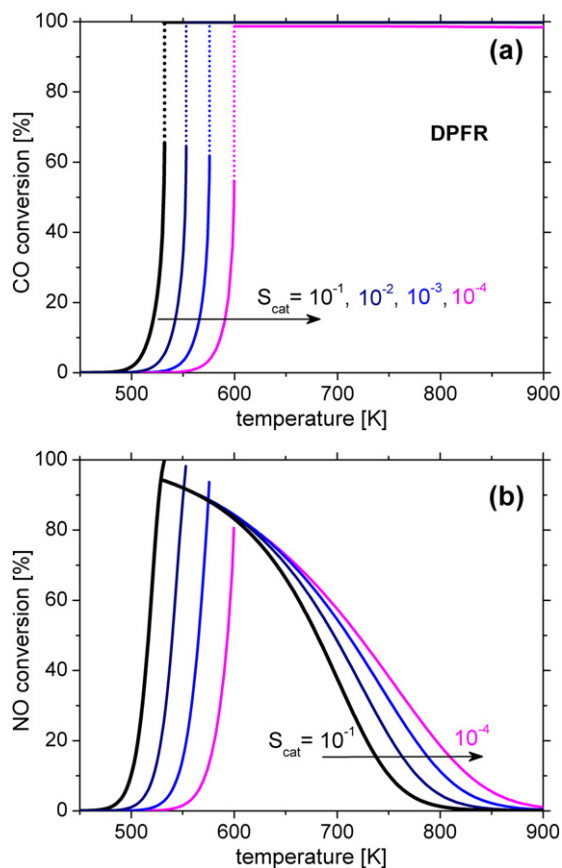
Fig. 8. Steady-state conversions of (a) CO and (b) NO as the functions of temperature for the DPFR model (using $N = 2 \times 10^3$) at different values of S_{cat} : 10^{-1} m^2 (black curve), 10^{-2} m^2 (navy), 10^{-3} m^2 (blue), 10^{-4} m^2 (magenta). (For interpretation of the references to color in this figure legend, the reader is referred to the web version of the article.)

Fig. 10. Steady-state conversion of NO versus temperature for the DPFR model ($N = 2 \times 10^3$), for two different values of S_{cat} : 10^{-1} m^2 (black curve), and 10^{-3} m^2 (blue curve). The Arrhenius parameters of the NO$_{ads}$ formation reaction are varied: (a) $E_9 = 110$ kJ/mol, $k_9^0 = 10^{13}$ s^{-1}; (b) $k_9 = 0$. (For interpretation of the references to color in this figure legend, the reader is referred to the web version of the article.)

seen that a decrease of E_9 from 130 down to 110 kJ/mol causes a significant change in the NO conversion only above the maximum NO-conversion temperature. When the NO$_{ads}$ formation reaction becomes faster, a decrease of $\eta_{NO}(T)$ at high temperatures proceeds more rapidly. In both cases, at elevated temperatures the catalyst with a small surface area may give better conversion of NO than the catalyst with a large surface area. It can be seen that this effect is more pronounced when the value of parameter k_9 increases. The effect disappears when $k_9 = 0$, as demonstrated in Fig. 10(b). If the
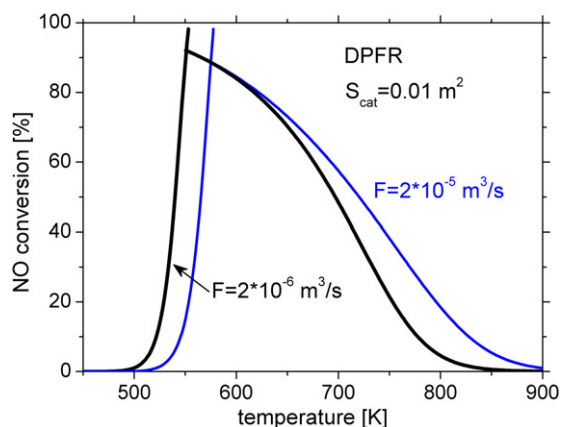
NO$_{ads}$ formation reaction is neglected, a monotonically increasing dependence of η_{NO} on S_{cat} is observed at all temperatures.

4. Conclusions

In general, the results of the DPFR model with realistic diffusion coefficients are qualitatively similar to those of the CSTR model. The most striking effect, predicted by these models for the NO + CO + O$_2$ catalytic reaction in a fixed-bed flow reactor, is the non-monotonic dependence of the NO conversion efficiency on S_{cat} and on F. In order to detect such dependence, the following important conditions are required: (1) the oxygen-rich reaction mixture; (2) the presence of the gas-phase diffusion; (3) a sufficiently high temperature; (4) a significant rate of the NO$_{ads}$ formation reaction. The ideal PFR model cannot reproduce this effect (if an accurate numerical method is applied).

As discussed in Ref. [12], the fall in NO conversion with increasing catalyst loading has been observed in numerous experiments concerning the reduction of NO by CO (and/or C$_x$H$_y$) under oxygen-rich conditions. As a rule, such experimental findings are considered as evidence that this reaction is "structure-sensitive". In this study, we presented the alternative explanations which are based on the peculiarities of the reaction mechanism in the case when the reaction is carried out in a fixed-bed flow reactor. These explanations are also applicable to other experiments in which the increase in the space velocity of the feed gas gives the increase in the NO conversion efficiency under isothermal steady-state operating conditions [13,14]. All these interesting

Fig. 9. Effect of the volumetric flow rate, F, on the steady-state NO conversion. The results were calculated using the DPFR model, $N = 2 \times 10^3$, $S_{cat} = 0.01$ m^2.
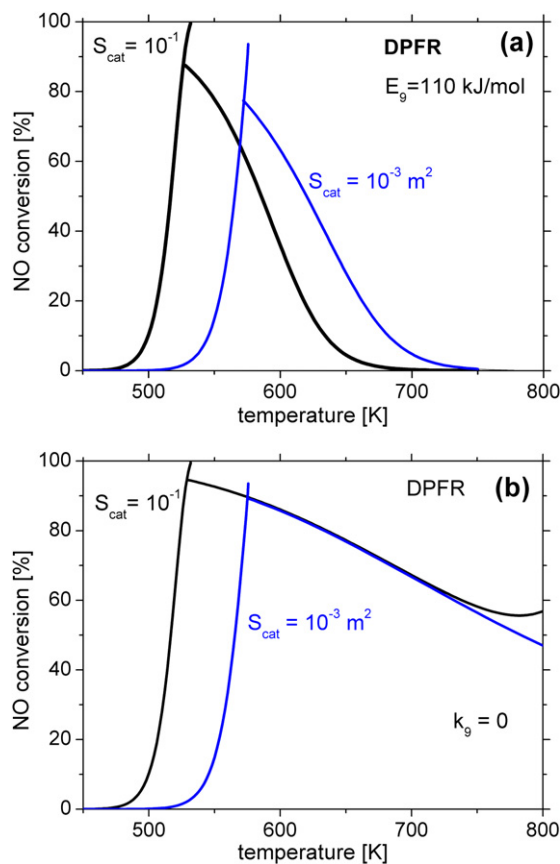
experimental findings can be qualitatively described using the DPFR model.

References

[1] R. Burch, J.P. Breen, F.C. Meunier, Applied Catalysis B: Environmental 39 (2002) 283.
[2] P. Granger, V.I. Parvulescu, Chemical Reviews 111 (2011) 3155.
[3] R.M. Lambert, C.M. Comrie, Surface Science 46 (1974) 61.
[4] G. Pirug, H.P. Bonzel, Journal of Catalysis 50 (1977) 64.
[5] S.H. Oh, G.B. Fisher, J.E. Carpenter, D.W. Goodman, Journal of Catalysis 100 (1986) 360.
[6] B.K. Cho, B.H. Shanks, J.E. Bailey, Journal of Catalysis 115 (1989) 486.
[7] Th. Fink, J.-P. Dath, R. Imbihl, G. Ertl, Journal of Chemical Physics 95 (1991) 2109.
[8] R. Burch, P.J. Millington, A.P. Walker, Applied Catalysis B: Environmental 4 (1994) 65.
[9] A.G. Makeev, B.E. Nieuwenhuys, Journal of Chemical Physics 108 (1998) 3740.
[10] D. Mei, Q. Ge, M. Neurock, L. Kieken, J. Lerou, Molecular Physics 102 (2004) 361.
[11] G. Novell-Leruth, J.M. Ricart, J. Pérez-Ramírez, Journal of Physical Chemistry C 112 (2008) 13554.
[12] A.G. Makeev, N.V. Peskov, H. Yanagihara, Applied Catalysis B: Environmental 119–120 (2012) 273.
[13] B.K. Cho, Journal of Catalysis 142 (1993) 418.
[14] B.K. Cho, J.E. Yie, Applied Catalysis B: Environmental 10 (1996) 263.
[15] P.A. Thiel, R.J. Behm, P.R. Norton, G. Ertl, Journal of Chemical Physics 78 (1983) 7448.
[16] K. Schwaha, E. Bechtold, Surface Science 66 (1977) 383.
[17] A. Eichler, Surface Science 498 (2002) 314.
[18] A. Eichler, J. Hafner, Journal of Catalysis 204 (2001) 118.
[19] M. Shimokawabe, N. Umeda, Chemistry Letters 33 (2004) 534.
[20] A. Kotsifa, D.I. Kondarides, X.E. Verykios, Applied Catalysis B: Environmental 80 (2007) 260.
[21] F.C. Meunier, V. Zuzaniuk, J.P. Breen, M. Olsson, J.R.H. Ross, Catalysis Today 59 (2000) 287.
[22] H. Inomata, M. Shimokawabe, M. Arai, Applied Catalysis A – General 332 (2007) 146.
[23] H.L. Abbott, I. Harrison, Journal of Physical Chemistry C 111 (2007) 13137.
[24] H.-J. Freund, M.W. Roberts, Surface Science Reports 25 (1996) 225.
[25] C.T. Goralski Jr., W.F. Schneider, Applied Catalysis B: Environmental 37 (2002) 263.
[26] H.B. Keller, Numerical solution of bifurcation and nonlinear eigenvalue problems, in: P. Rabinowitz (Ed.), Applications of Bifurcation Theory, Academic Press, New York, 1977.
[27] A.G. Makeev, N.L. Semendyaeva, Computational Mathematics and Mathematical Physics 49 (2009) 623.
[28] R.H. Nibbelke, J.H.B.J. Hoebink, G.B. Marin, Chemical Engineering Science 53 (1998) 2195.
[29] M. Kim, S.J. Pratt, D.A. King, Journal of the American Chemical Society 122 (2000) 2409.
[30] C.J. Weststrate, J.W. Bakker, E.D.L. Rienks, C.P. Vinod, A.V. Matveev, V.V. Gorodetskii, B.E. Nieuwenhuys, Journal of Catalysis 242 (2006) 184.
[31] D. Chatterjee, O. Deutschmann, J. Warnatz, Faraday Discussions 119 (2001) 371.
[32] E.V. Rebrov, M.H.J.M. de Croon, J.C. Schouten, Chemical Engineering Journal 90 (2002) 61.
[33] Y.W. Budhi, A. Jaree1, J.H.B.J. Hoebink, J.C. Schouten, Chemical Engineering Science 59 (2004) 4125.
[34] A. Scheibe, M. Hinz, R. Imbihl, Surface Science 576 (2005) 131.
[35] M. Rafti, J.L. Vicente, A. Albesa, A. Scheibe, R. Imbihl, Surface Science 606 (2012) 12.
[36] A. Scheuer, W. Hauptmann, A. Drochner, J. Gieshoff, H. Vogel, M. Votsmeier, Applied Catalysis B: Environmental 111–112 (2012) 445.